Anhydrous Grotthuss mechanism for fast proton transport in a dense oxide-ion array of α-MoO_3

Zihan Ma
https://orcid.org/0000-0002-4169-0605
Xiang-Mei Shi
The University of Tokyo https://orcid.org/0000-0003-3198-2660
Shin-ichi Nishimura
The University of Tokyo https://orcid.org/0000-0001-7464-8692
Seongjae Ko
The University of Tokyo
Masashi Okubo
Waseda University
Atsuo Yamada (yamada@chemsys.t.u-tokyo.ac.jp)
The University of Tokyo https://orcid.org/0000-0002-7880-5701

Article

Keywords:

Posted Date: January 13th, 2022

DOI: https://doi.org/10.21203/rs.3.rs-1201760/v1

Version of Record: A version of this preprint was published at Advanced Materials on July 4th, 2022. See the published version at https://doi.org/10.1002/adma.202203335.

Abstract

Developing high-power battery chemistry is an urgent task to buffer fluctuating renewable energies and achieve a sustainable and flexible power supply. Owing to the small size of proton and its ultrahigh mobility in water *via* the Grotthuss mechanism, aqueous proton batteries are an attractive candidate for high-power energy storage devices. Although Grotthuss proton transfer usually occurs in hydrogen-bonded networks of water molecules, in this work, we discover anhydrous Grotthuss-type proton transport in a dense oxide-ion array of solid α-MoO_3 even without structural water. The fast proton transfer and accumulation that occurs during (de)intercalation in α-MoO_3 is unveiled using both experiments and first-principles calculations. Coupled with a zinc anode and a superconcentrated dual-ion Zn^{2+}/H^+ electrolyte, the solid-state anhydrous Grotthuss proton transport mechanism realizes an aqueous MoO_3-Zn battery with both high energy and power densities.

Main

The increasing concern given to the global environment and energy sustainability is driving the research and development of electrochemical energy storage devices that provide power supply with more resilience and flexibility. Currently, lithium-ion batteries dominate the power-source market for portable devices and electric vehicles due to their high energy density, high energy efficiency, and long lifetime.[1,2] However, the global maldistribution of lithium resources has impeded their further widespread use.[3] In particular, flammable organic electrolytes in lithium-ion batteries result in a low safety level and high fabrication/maintenance costs, both of which are unacceptable for grid-scale use.[4] Therefore, aqueous rechargeable batteries that contain safe and less expensive aqueous electrolytes are an important future alternative for sustainable development.[5]

For the development of aqueous batteries with high energy density, exploiting Zn metal as a negative electrode is a straightforward approach because the Zn metal electrode possesses high theoretical capacities of 820 mAh/g and 5854 mAh/L. While reversible Zn metal plating/stripping is an important issue to be addressed for the development of aqueous Zn-ion batteries[6], another large challenge also remains in a positive electrode. The intercalation of large hydrated Zn^{2+} generally causes damaging structural changes upon charge/discharge, leading to capacity degradation after cycling.[7] Consequently, the concept of aqueous dual-ion batteries has recently been increasingly studied. For example, an aqueous Zn^{2+}/Li^+ dual-ion battery, which consists of a Zn metal plating/stripping negative electrode and Li^+ intercalation positive electrode (e.g., $LiFePO_4$) with an aqueous dual-ion Zn^{2+}/Li^+ electrolyte, was reported to provide an energy density of approximately 95 Wh/kg with 90% capacity retention after 80 cycles[8].

In this work, we focus on protons as charge carriers in aqueous dual-ion batteries (**Figure 1**). Proton is the smallest and lightest cation; thus, it can be easily (de)intercalate in various structures at a fast rate.[9] Moreover, barrierless H^+ hopping enables fast H^+ transport in an electrolyte owing to the Grotthuss

mechanism, where protons are transferred through the hydrogen bond network.[10] In recent years, the Grotthuss topochemistry was extended to hydrate solid-state materials; for example, Prussian blue analogs exhibit fast H^+ (de)intercalation with the assistance of structural water networks.[11] Similarly, the intercalated water layers in transition metal carbide nanosheets (MXenes) facilitate H^+ storage and fast H^+ transfer.[12,13] Without structural/confined water, quinone-based organic compounds, which store H^+ on carbonyl groups, exhibit both long cycle lives and large capacities.[14]

Among various transition metal (TM) oxides (TM= Mn, V, W, Ti, Mo)[15–24] that deliver large capacities upon protonation, orthorhombic MoO_3 (α-MoO_3) possesses a unique bilayered structure (**Figure 1**) that accommodates various cations, such as Li^+[25,26], Na^+[27], Ca^{2+}[28] and Mg^{2+}[29] in organic electrolytes. In aqueous electrolytes, the intercalation of bare Zn^{2+}[30,31] and Al^{3+}[32] has also been studied. However, the H^+ intercalation behavior in α-MoO_3 with various aqueous electrolytes remains controversial: some reports claim a bare H^+ intercalation mechanism[33–37] that is consistent with H_xMoO_3 bronze obtained through the spillover method[38], while others report water and H^+ cointercalation[39,40]. Meanwhile, α-MoO_3 suffers severe dissolution in aqueous electrolytes; therefore, the capacity decays gradually upon cycling, making it difficult to study the detailed H^+ intercalation mechanism. Although many attempts have been made to solve this issue, for example, the use of highly concentrated electrolytes[40,41], gel-type or quasi-solid-state electrolytes with polymer additives[31], and electrode surface coating with polymers or ceramics[30,42], the detailed H^+ intercalation mechanism in α-MoO_3 has yet to be fully understood. Herein, we provide the full comprehension of H^+ intercalation in α-MoO_3 as a cathode material for aqueous Zn^{2+}/H^+ batteries. Fast H^+ transfer in α-MoO_3 through a solid-state anhydrous Grotthuss mechanism realizes aqueous batteries with both high power and high energy densities.

Electrochemical properties of MoO_3 in aqueous Zn^{2+}/H^+ electrolytes

α-MoO_3 was synthesized by a previously reported hydrothermal method,[40] and the synchrotron X-ray diffraction pattern confirmed the successful synthesis of a pure α-MoO_3 phase (**Figure S1**). To study the H^+ intercalation mechanism in α-MoO_3, $ZnCl_2$ was selected as an electrolyte salt. In addition to its compatibility with a Zn anode, the high solubility of $ZnCl_2$ enabled the formation of a superconcentrated liquid structure with limited amount of free water molecules, while its Brønsted acidity generated a low pH environment with a high H^+ concentration. Therefore, the electrochemical properties of α-MoO_3 were evaluated using three aqueous electrolytes: conventional Zn^{2+} electrolyte (3 mol kg^{-1} $ZnCl_2/H_2O$), superconcentrated Zn^{2+} electrolyte (32 mol kg^{-1} $ZnCl_2/H_2O$), and superconcentrated dual-ion (Zn^{2+}/H^+) electrolytes (32 mol kg^{-1} $ZnCl_2$ + 1 mol kg^{-1} P_2O_5/H_2O). Note that P_2O_5 in a dual-ion electrolyte

generates H^+ through hydrolysis ($P_2O_5 + 3H_2O \rightarrow 2H_3PO_4$). The Raman spectra for the superconcentrated electrolytes indicate that most water molecules are coordinated to Zn^{2+} (**Figure S2**).

Before testing the electrochemical properties of α-MoO_3, we evaluated the negative electrode, namely, Zn stripping and plating on a Ti current collector using the three electrolytes (**Figures S3** and **2a**).[6] The average coulombic efficiency in the aqueous Zn^{2+}/H^+ dual-ion electrolyte is 99.0% over 200 cycles (**Figure S3**), largely outperforming the superconcentrated Zn^{2+} electrolyte (95.0% over 200 cycles) and conventional Zn^{2+} electrolyte (82.2% over 100 cycles). The improved zinc reversibility after the addition of P_2O_5 may result from the formation of a $Zn_3(PO_4)_2$-based solid electrolyte interphase (SEI) layer.[43] This reversible Zn stripping and plating was used as the counter electrode in this work.

Figure 2b shows the cyclic voltammetry (CV) curves measured for α-MoO_3 using the three electrolytes at a scan rate of 0.5 mV s^{-1}. To suppress the hydrogen evolution and chlorine evolution reactions on the α-MoO_3 electrode, the cutoff voltages were set at 0.45 and 1.3 V for the aqueous Zn^{2+}/H^+ dual-ion electrolyte (**Figure 2a**) and 0.25 and 1.1 V for the Zn^{2+} aqueous electrolytes. In the first CV cycle (**Figure 2b** inset), the α-MoO_3 electrode shows identical asymmetric-shaped CV curves for all three electrolytes, in which there are four cathodic and two anodic current flows. However, in the subsequent cycles, the CV curves become symmetric, showing two pairs of redox peaks. Note that the redox potentials using the aqueous Zn^{2+}/H^+ dual-ion electrolyte are centered at approximately 0.6 and 0.95 V *vs.* Zn/Zn^{2+}, which shift by +0.2 V from those using Zn^{2+} aqueous electrolytes presumably owing to the potential shift of the Zn/Zn^{2+} counter electrode and/or the change in the activity of H^+. The shapes of the CV curves for all three electrolytes resemble those reported for H^+ (de)intercalation in α-MoO_3 using a 9.5 M H_3PO_4 aqueous electrolyte[40], suggesting dominant H^+ (de)intercalation even when using the Zn^{2+} aqueous electrolytes. Indeed, the X-ray fluorescence (XRF) elemental analysis of the electrodes after a cathodic scan shows no evident increase in the peak intensity of Zn compared to that of the pristine electrode (**Figure. S4**). Considering that the aqua Zn^{2+} complex is a Brønsted acid to generate H^+, it is most likely that H^+ (de)intercalation occurs even when using the aqueous Zn^{2+} electrolytes. Importantly, while 3 and 32 mol kg^{-1} $ZnCl_2$ aqueous electrolytes exhibit steep redox peak degradation upon repeated CV cycling, the 32 mol kg^{-1} $ZnCl_2$ + 1 mol kg^{-1} P_2O_5 aqueous dual-ion electrolyte exhibits stable CV curves (**Figure 2b**). The improved cycle stability should be ascribed to the suppression of α-MoO_3 dissolution and the formation of effective SEI.[43] Indeed, the X-ray photoelectron spectroscopy (XPS) analysis of the Zn metal anode after cycling in the 3 m $ZnCl_2$ electrolyte evidences the Mo deposition from the Mo ions dissolved in the electrolyte (**Figure S6**).

Figure 2c shows the charge/discharge curves of the α-MoO_3 electrode with galvanostatic charging followed by 3 h of potentiostatic charging in the aqueous Zn^{2+}/H^+ dual-ion electrolyte. The α-MoO_3

electrode delivers a large capacity of 465 mAh g^{-1} at a rate of 0.5 A g^{-1} during the first discharge, corresponding to 2.5 H^+ intercalation per formula unit of MoO_3 with an average voltage of approximately 0.9 V. Note that 'discharge' and 'charge' of the α-MoO_3 electrode are defined as H^+ intercalation (cathodic process) and deintercalation (anodic process), respectively. Although the galvanostatic charge at 0.5 A g^{-1} can extract only 1.5 H^+, the remaining 1.0 H^+ can be extracted when applying a constant voltage of 1.3 V for 3 h (**Figures S7** and **S8**). The diffusion coefficient determined by the potentiostatic intermittent titration technique (PITT) shows a significant 4.9-fold deceleration in H^+ diffusion during the deprotonation from $H_{1.1}MoO_3$ to MoO_3, confirming the trapped nature of ~1.0 H^+ in MoO_3 (**Figure S9**).

Under galvanostatic charging (without a potentiostatic step), the α-MoO_3 electrode in an aqueous Zn^{2+}/H^+ dual-ion electrolyte retains 98% of its initial capacity after 1000 cycles at a rate of 2 A g^{-1} (**Figure 3a**). Furthermore, 62% of the specific capacity at 1 A g^{-1} is available at the fast discharge rate of 16 A g^{-1} (**Figure 3b** and **Figure S10**). These performance results indicate the stability of the MoO_3 framework against (de)protonation as well as the fast proton diffusion therein H_xMoO_3 ($1.0 \leq x \leq 2.5$). In contrast, the α-MoO_3 electrodes in the aqueous Zn^{2+} electrolytes have capacity retentions of only 24.5% and 63.8%, respectively (**Figures S11** and **S12**). Moreover, both the capacity and cycling stability of the α-MoO_3 electrode in the aqueous Zn^{2+}/H^+ dual-ion electrolyte outperform those reported previously for α-MoO_3 electrodes using aqueous electrolytes, including quasi-solid-state Zn^{2+} electrolytes[30,31] and concentrated acid electrolytes[33,40].

MoO_3 host-lattice response to proton intercalation

To clarify the structural evolution of the α-MoO_3 electrode in the aqueous Zn^{2+}/H^+ dual-ion electrolyte, *in situ* X-ray diffraction (XRD) was performed during the 1st cycle (**Figure 4a**). The interlayer distance of α-MoO_3 remains nearly constant (approximately 7.0 Å) during the entire protonation process, while it increases from 7.0 to 7.5 Å and then decreases to 7.0 Å during deprotonation. This asymmetric lattice response is consistent with the asymmetric CV and charge/discharge curves, which also highly resemble those reported in a 6 M H_2SO_4 electrolyte[33] and in a 4.4 M H_2SO_4 electrolyte[35]. However, despite the asymmetric structural evolution, the α-MoO_3 structure recovers to the pristine state after a constant voltage is applied. The structure of the fully protonated phase was clarified using *ex situ* synchrotron XRD and Rietveld refinement (**Figure 4b** and **4c**). Although it is difficult to determine proton positions using X-rays, the MoO_3 framework only exhibits a slight monoclinic distortion after protonation, which is consistent with a previous report on $H_{1.68}MoO_3$[44] and the *in situ* XRD results.

Importantly, no water cointercalation occurs in the protonated structure. When a small amount of water (one water or hydronium intercalation in 16 formula units of MoO_3) is intercalated, the density functional theory (DFT) calculation predicts that the interlayer distance expands by 13.8% (H_2O intercalation) and

17.2% (H_3O^+ intercalation) (**Figure S13**), which are considerably larger than those observed experimentally. Additionally, the interlayer distance after water cointercalation in a 1 M H_2SO_4 electrolyte has been reported to show an expansion of 11% upon protonation[39], in contrast to the negligible change observed in the protonation process in our experiment. Therefore, bare H^+ (de)intercalation occurs in the α-MoO_3 electrode with the aqueous Zn^{2+}/H^+ electrolyte.

Solid-state anhydrous Grotthuss mechanism

The above experimental results indicate asymmetric bare-H^+ (de)intercalation in the α-MoO_3 electrode. To clarify the origin of this asymmetry, we conducted DFT calculations on the H^+ dynamics in α-MoO_3. The stable sites for H^+ were determined by the structural optimization of the protonated phases. The three most stable H^+ absorption sites are labeled as site A (O2-H···O2), site B (O1-H···O1/O2) and site C (O2-H···O1), where O1 and O2 are the terminating oxygen coordinated to one Mo and the bridging oxygen coordinated to two Mo, respectively (**Figure S14**). The remaining edge-sharing oxygen (O3) coordinated to three Mo atoms is not favorable for H^+ adsorption because all O 2*p* orbitals (2p_x, 2p_y, and 2p_z) participate in the Mo 4*d*-O 2*p* bonds. Site A is located within the MoO_3 layer, while sites B and C are located in the MoO_3 interlayer space.

The most favorable site for H^+ changes as a function of x in H_xMoO_3. At low H^+ concentrations during protonation ($0 < x \leq 0.5$ in H_xMoO_3), intralayer site A is the most favorable for H^+ adsorption. However, after 0.5 H^+ intercalation ($0.5 < x \leq 2.5$ in H_xMoO_3), interlayer sites B and then C become more favorable than site A, leading to the final formula of $H_{2.5}MoO_3$ (site A (0.5 H^+) → site B (1.5 H^+) → site C (0.5 H^+), **Figure 5a** and **Figure S15**). Further protonation of site B (H_3MoO_3) is not thermodynamically favored, as it causes structural decomposition.

On the other hand, at the early stage of deprotonation ($2.5 > x \geq 2.25$ in H_xMoO_3), the DFT calculations suggest that 0.25 H^+ is extracted from interlayer site C. Then, for $2.25 > x \geq 1.5$ in H_xMoO_3, 0.5 H^+ at site A is predominantly deintercalated in addition to the simultaneous partial deintercalation of H^+ at site B. After completing H^+ deintercalation from site A, the H^+ at site B is deintercalated ($1.5 > x \geq 0$ in H_xMoO_3). In parallel, the remaining 0.25 H^+ at site C is deintercalated at the end of deprotonation. Notably, the deprotonation order (site C (0.25 H^+) → site A (0.5 H^+) → site B (0.75 H^+) → site B + site C (1.0H^+)) (**Figure 5b**) does not follow the protonation order (site A (0.5 H^+) → site B (1.5 H^+) → site C (0.5 H^+)), which explains the asymmetric charge/discharge profile. Experimentally, complete deprotonation is possible only when a constant voltage is applied (**Figure 2c**). The sluggish deprotonation at the end of charging may arise from the slow kinetics of the remaining H^+ at sites B and C. The calculated voltage profile agrees well with the experimental results, confirming the validity of the asymmetric (de)protonation processes (**Figure S16**).

To unveil the origin of the facile (de)protonation in the $1.0 < x \leq 2.5$ range of H_xMoO_3 and the sluggish deprotonation in the $1.0 \geq x \geq 0$ range of H_xMoO_3, climbing image nudged elastic band (CI-NEB) calculations were conducted, and the energy profile of H^+ diffusion in MoO_3 was visualized (**Figure 5c**). At the beginning of protonation, H^+ rotates and hops consecutively between site A with a low energy barrier of 0.13 eV. The dense, zigzagged O2 (bridging oxygen) array provides a 1D channel for fast proton transport within the MoO_3 intralayer space, where the short O2-O2 distance (2.63 Å) facilitates proton hopping. Upon the further protonation of $H_{0.5}MoO_3$, the interlayer diffusion channel containing site B also has a low energy barrier of 0.26 eV with an O1-O1/O2 distance of 2.71 Å (**Figure S17**), confirming the high mobility of H^+ at site B.

As shown in **Figure 5d**, the deprotonation from site C of $H_{2.5}MoO_3$ also involves a small energy barrier of 0.29 eV through the interlayer diffusion channel containing sites B and C (O-O distance of 2.86 Å). The H^+ transfer in the dense oxide-ion array is described as the solid-state anhydrous Grotthuss mechanism, whose kinetics highly rely on the distance between two adjacent lattice oxide ions. **Figure S18** summarizes the statistics of O-O distances in all possible deprotonation channels of the charged structures. As expected, during deprotonation from $H_{2.5}MoO_3$ to $HMoO_3$, short O-O distances of < 2.9 Å exist to enable solid-state anhydrous Grotthuss H^+ transfer. However, after extracting 0.25 H^+ from site C in $H_{2.5}MoO_3$, the O-O distances in the diffusion channel consisting of sites B and C increase drastically (> 3.1 Å); meanwhile, the energy barrier therein for H^+ diffusion becomes remarkably high (0.98 eV, **Figure S19**). Therefore, further deprotonation from site C is unfavorable, instead, protons in site A are deintercalated, resulting in asymmetric (de)protonation (**Figure 5b**). Indeed, after deprotonation to $HMoO_3$, all the long-range 1D channels are disrupted so that fast Grotthuss H^+ transfer is no longer applicable (**Figure S20**). The remaining H^+ can be removed only under long relaxation times, such as potentiostatic charging and PITT (**Figure S21** and **S22**). However, except for the trapped H^+ at site C, H_xMoO_3 ($1.0 \leq x \leq 2.5$) exhibits fast H^+ transport through the diffusion channels upon charge/discharge, providing a remarkably high capacity and high-rate capability, as demonstrated in **Figure 3**.

To summarize, coupled with a zinc metal anode and an aqueous dual-ion Zn^{2+}/H^+ (32 m $ZnCl_2$ + 1 m P_2O_5) electrolyte, the MoO_3-Zn battery delivers a large energy density of 413 Wh kg^{-1} upon discharge at a power density of 0.90 kW kg^{-1} as well as a peak power density of 10.52 kW kg^{-1} at an energy density of 217 Wh kg^{-1} per weight of MoO_3; these results are more than double that of a similar MoO_3-Zn battery with a $ZnCl_2$-based electrolyte[39] (energy density of 198 Wh kg^{-1} at a power density of 0.28 kW kg^{-1} and power density of 6.7 kW kg^{-1} at an energy density of 104.5 Wh kg^{-1}). Moreover, with the aid of the solid-state anhydrous Grotthuss mechanism, this prototype cell successfully outperforms most aqueous zinc-ion batteries and proton batteries (**Figure S23**). Contrary to conventional intercalation chemistry, which requires a porous host that accommodates ion diffusion and storage, the solid-state anhydrous Grotthuss mechanism demonstrated in this work enables fast H^+ transfer and accumulated H^+ storage in dense oxide-ion arrays. Therefore, further exploration for other host materials capable of H^+

intercalation based on the solid-state anhydrous Grotthuss mechanism will be an important challenge for not only fabrications of high-power aqueous H^+ batteries but also other solid-state ionics applications using protons.

Methods

α-MoO_3 was synthesized *via* a simple hydrothermal synthesis approach[40], where 1 g of $(NH_4)_6Mo_7O_{24}{\cdot}4H_2O$ (Wako) was dissolved in 25 mL of water, followed by the addition of 10 mL of HNO_3 solution (3 M). After stirring for 10 min, the transparent colorless solution was poured into a 50 mL Teflon™-lined Parr autoclave and heated at 180 °C for 12 h. After filtration, the white-colored powder was washed with water and ethanol and then dried in an oven at 80 °C in air overnight.

The electrolyte was prepared by weighing $ZnCl_2$ and P_2O_5 in an argon-filled glovebox to prevent the absorption of water. After weighing, ultrapure water (Wako) was mixed with salts to form a solution in open air.

The working electrode for electrochemical characterization was formulated by slurry casting 70 wt% MoO_3 active material, 20 wt% Ketjen-black (ECP-600JD, Lion Corp.) and 10 wt% polyvinylidene difluoride (PVDF) binder on Ti foil or carbon paper (for *in situ* X-ray diffraction (XRD)) using prompt amounts of N-methyl-2-pyrrolidone (NMP) (Kanto, 99%) as the solvent. The loading level of the electrodes was controlled to ~1 mg cm^{-2}.

The electrochemical performance was tested in PTFE three-electrode beaker cells with Ag/AgCl (in a saturated KCl aqueous solution) as the reference electrode and activated carbon as the counter electrode. In the two-electrode cell tests, zinc foil was attached to a titanium wire, working as both the reference and counter electrode. The zinc stripping and plating tests were conducted in a 2032-type coin cell where a titanium foil and a zinc foil were separated with a glass fiber separator (Fisher) presoaked with an electrolyte. The *in situ* XRD studies were conducted in a custom cell with a Kapton® membrane window on the cathode side.

The electrochemical performance was studied *via* cyclic voltammetry (CV) and galvanostatic charge and discharge (GCD), the galvanostatic intermittent titration technique (GITT) and the potentiostatic intermittent titration technique (PITT) using a VMP3 potentiostat (BioLogic) at room temperature.

Powder XRD and *in situ* XRD studies were conducted with a Bruker-AXS D8 ADVANCE diffractometer using a Co sealed tube (operating at 35 kV, 40 mA) and a linear position-sensitive detector (LYNX-EYE). VESTA[45] software was used to illustrate the crystal structure. For crystal structure refinement, we used a powder diffractometer at a synchrotron radiation beamline 5S2 of Aichi Synchrotron Radiation Center,

Japan. The wavelength used was calibrated by refining a powder diffraction pattern of the ceria power, and the value was 0.700072(9) Å.

Elemental analysis of the MoO_3 electrodes by energy dispersive X-ray fluorescence (XRF) spectroscopy was performed with a JSX-3400RII instrument (JEOL).

The surface chemistry of the Zn electrodes was analyzed *via* X-ray photoelectron spectroscopy (XPS, PHI5000 VersaProbe II, ULVAC-PHI) with a monochromatic Al K_X-ray source. The Zn electrode samples were rinsed with pure water and acetone after being extracted from cycled cells.

The coordination states of the water molecules were investigated by Raman spectroscopy (NRS-5100, JASCO). A 532 nm excitation laser was used. The electrolyte solution was sealed in a quartz cell, and the laser was directed through the quartz crystal window.

Spin-polarized DFT calculations were carried out using the Vienna ab initio simulation package (VASP).[46,47] The projector-augmented wave pseudopotential and a plane-wave basis set with an energy cutoff of 520 eV were used.[48] The Perdew-Burke-Ernzerhof functional[49,50] with the Grimme scheme D2[51] described the exchange-correlation energy, and the Hubbard U correction was applied to the d electrons of the Mo atoms (U_{eff} = 3.5 eV).[52] A k-point separation of approximately 0.04 $Å^{-1}$ was used in all calculations.

Based on a 2 × 1 × 2 supercell ($Mo_{16}O_{48}$), we calculated a series of H-intercalated structures of H_xMoO_3 ($0 \leq x \leq 3.0$). Each proton was placed between two nearby O atoms where one covalent bond (~1 Å) and one hydrogen bond (1.6~2.3 Å) were formed. All possible configurations were calculated by optimizing both the lattice and ion positions, and then we constructed a convex hull to identify the stable phases in the discharge and charge processes. The formation energies (at 0 K) were calculated as:

$$\Delta E_f(H_xMoO_3) = E(H_xMoO_3) - \frac{(3-x)}{3}E(MoO_3) - \frac{x}{3}E(H_3MoO_3) \quad (1)$$

where $E(H_xMoO_3)$, $E(MoO_3)$ and $E(H_3MoO_3)$ are the total energies of H_xMoO_3, pristine MoO_3 and H_3MoO_3 (maximally H-intercalated configuration), respectively. The determined structures are shown in Supplementary **Figure S19**. The voltage profile was then evaluated, with the average voltage of the reaction between two adjacent stable phases calculated as:

$$U(x_1, x_2) = -[E(H_{x_1}MoO_3) - E(H_{x_2}MoO_3) - (x_1 - x_2)\mu_H]/(x_1 - x_2)F \quad (2)$$

where F is the Faraday constant, μ_H is the chemical potential of hydrogen gas at atmospheric pressure, and T = 298.15 K.

$$\mu_H = E(H_2) + 7/2\ k_B T - T\Delta S \quad (3)$$

In the above equation, $E(H_2)$ is the calculated total energy of a hydrogen molecule, k_B is the Boltzmann constant and ΔS is obtained from the JANAF thermochemistry tables.[53]

We used the climbing image nudged elastic band (CI-NEB) method to calculate proton diffusion pathways in $a\ 2\sqrt{2} \times 1 \times 2\sqrt{2}$ supercell.[54] For the stable structures in the discharge process, an extra proton was added to migrate between two neighboring adsorption sites. In the charge process, a proton was removed from the stable structures to construct a vacancy site for the migration of other protons.

Declarations

Author Contributions

M.O. and A.Y. conceived and directed the project. Z.M. conducted material synthesis and electrochemical measurements. Z.M. and X.M.S. conducted the theoretical calculations. S.N. conducted the structural analysis. Z.M. and S.K. designed the experiments. All authors wrote the manuscript.

Conflicts of Interest

There are no conflicts of interest.

Acknowledgments

This work was financially supported by JST CREST grant no. JPMJCR21O6. This work was also supported by the Ministry of Education, Culture, Sports, Science and Technology (MEXT), Japan; Grant-in-Aid for Scientific Research (S) no. 20H05673. M.O. was financially supported by Grant-in-Aid for Scientific Research (A) no. 21H04697 and Grant-in-Aid for Scientific Research on Innovative Areas 19H05816. The computation in this work was performed at the Supercomputer Center, Institute for Solid State Physics, the University of Tokyo. The powder diffraction experiments using synchrotron radiation were conducted at a beamline 5S2 of Aichi Synchrotron Radiation Center, Japan (proposal nos. 2020D5045 and 2020D4002). Z.M. acknowledges the Global Leader Program for Social Design and Management for her grant.

References

1. Armand, M. & Tarascon, J.-M. Building better batteries. *Nature* **451**, 652–657 (2008).

2. Tarascon, J.-M. & Armand, M. Issues and challenges facing rechargeable lithium batteries. *Nature* **414**, 359–367 (2001).
3. Tarascon, J.-M. Is lithium the new gold? *Nature Chemistry* **2**, 510–510 (2010).
4. Xu, K. Nonaqueous Liquid Electrolytes for Lithium-Based Rechargeable Batteries. *Chem. Rev.* **104**, 4303–4418 (2004).
5. Yamada, Y. *et al.* Hydrate-melt electrolytes for high-energy-density aqueous batteries. *Nature Energy* **1**, 1–9 (2016).
6. Ma, L. *et al.* Realizing high zinc reversibility in rechargeable batteries. *Nature Energy* **5**, 743–749 (2020).
7. Li, H. *et al.* Advanced rechargeable zinc-based batteries: Recent progress and future perspectives. *Nano Energy* **62**, 550–587 (2019).
8. Mainar, A. R., Iruin, E. & Blázquez, J. A. New Insights of Zn^{2+}/Li^{+} Hybrid Aqueous Batteries. *Energy Technology* **8**, 2000476 (2020).
9. Xu, Y., Wu, X. & Ji, X. The Renaissance of Proton Batteries. *Small Structures* **2**, 2000113 (2021).
10. Agmon, N. The Grotthuss mechanism. *Chemical Physics Letters* **244**, 456–462 (1995).
11. Wu, X. *et al.* Diffusion-free Grotthuss topochemistry for high-rate and long-life proton batteries. *Nature Energy* **4**, 123–130 (2019).
12. Sun, Y. *et al.* Proton Redox and Transport in MXene-Confined Water. *ACS Appl. Mater. Interfaces* **12**, 763–770 (2020).
13. Lukatskaya, M. R. *et al.* Ultra-high-rate pseudocapacitive energy storage in two-dimensional transition metal carbides. *Nature Energy* **2**, 1–6 (2017).
14. Liang, Y. *et al.* Universal quinone electrodes for long cycle life aqueous rechargeable batteries. *Nature Materials* **16**, 841–848 (2017).
15. Sun, W. *et al.* Zn/MnO_2 Battery Chemistry With H^{+} and Zn^{2+} Coinsertion. *J. Am. Chem. Soc.* **139**, 9775–9778 (2017).
16. Zhao, Q. *et al.* Boosting the Energy Density of Aqueous Batteries via Facile Grotthuss Proton Transport. *Angewandte Chemie* **133**, 4215–4220 (2021).
17. Zhao, Q. *et al.* Proton Intercalation/De-Intercalation Dynamics in Vanadium Oxides for Aqueous Aluminum Electrochemical Cells. *Angewandte Chemie International Edition* **59**, 3048–3052 (2020).
18. Lin, H., Zhou, F., Liu, C.-P. & Ozoliņš, V. Non-Grotthuss proton diffusion mechanism in tungsten oxide dihydrate from first-principles calculations. *Journal of Materials Chemistry A* **2**, 12280–12288 (2014).
19. Jiang, H. *et al.* Insights on the Proton Insertion Mechanism in the Electrode of Hexagonal Tungsten Oxide Hydrate. *J. Am. Chem. Soc.* **140**, 11556–11559 (2018).
20. Betz, G., Tributsch, H. & Marchand, R. Hydrogen insertion (intercalation) and light induced proton exchange at TiO_2(B) -electrodes. *J Appl Electrochem* **14**, 315–322 (1984).

21. Fabregat-Santiago, F. *et al.* High Carrier Density and Capacitance in TiO_2 Nanotube Arrays Induced by Electrochemical Doping. *J. Am. Chem. Soc.* **130**, 11312–11316 (2008).
22. Birtill, J. J. & Dickens, P. G. Phase relationships in the system H_xMoO_3 ($0<x\leq2.0$). *Materials Research Bulletin* **13**, 311–316 (1978).
23. Schöllhorn, R., Kuhlmann, R. & Besenhard, J. O. Topotactic redox reactions and ion exchange of layered MoO3 bronzes. *Materials Research Bulletin* **11**, 83–90 (1976).
24. Parise, J. B., McCarron, Eugene. M. & Sleight, A. W. A new modification of ReO_3-type MoO_3 and the deuterated intercalation compound from which it is derived: $D_{0.99}MoO_3$. *Materials Research Bulletin* **22**, 803–811 (1987).
25. Mai, L. Q. *et al.* Lithiated MoO_3 Nanobelts with Greatly Improved Performance for Lithium Batteries. *Advanced Materials* **19**, 3712–3716 (2007).
26. Zhou, L. *et al.* α-MoO_3 Nanobelts: A High Performance Cathode Material for Lithium Ion Batteries. *J. Phys. Chem. C* **114**, 21868–21872 (2010).
27. Hariharan, S., Saravanan, K. & Balaya, P. α-MoO_3: A high performance anode material for sodium-ion batteries. *Electrochemistry Communications* **31**, 5–9 (2013).
28. Cabello, M. *et al.* Applicability of Molybdite as an Electrode Material in Calcium Batteries: A Structural Study of Layer-type Ca_xMoO_3. *Chem. Mater.* **30**, 5853–5861 (2018).
29. Spahr, M. E., Novák, P., Haas, O. & Nesper, R. Electrochemical insertion of lithium, sodium, and magnesium in molybdenum(VI) oxide. *Journal of Power Sources* **54**, 346–351 (1995).
30. Liu, Y. *et al.* Interfacial Engineering Coupled Valence Tuning of MoO_3 Cathode for High-Capacity and High-Rate Fiber-Shaped Zinc-Ion Batteries. *Small* **16**, 1907458 (2020).
31. He, X. *et al.* Stabilized Molybdenum Trioxide Nanowires as Novel Ultrahigh-Capacity Cathode for Rechargeable Zinc Ion Battery. *Advanced Science* **6**, 1900151 (2019).
32. Lahan, H. & Das, S. K. Al^{3+} ion intercalation in MoO_3 for aqueous aluminum-ion battery. *Journal of Power Sources* **413**, 134–138 (2019).
33. Su, Z. *et al.* Ultrahigh Areal Capacity Hydrogen-Ion Batteries with MoO_3 Loading Over 90 mg cm^{-2}. *Advanced Functional Materials* **30**, 2005477 (2020).
34. Wang, X., Xie, Y., Tang, K., Wang, C. & Yan, C. Redox Chemistry of Molybdenum Trioxide for Ultrafast Hydrogen-Ion Storage. *Angewandte Chemie International Edition* **57**, 11569–11573 (2018).
35. Guo, H. *et al.* Two-Phase Electrochemical Proton Transport and Storage in α-MoO_3 for Proton Batteries. *Cell Reports Physical Science* **1**, 100225 (2020).
36. Deng, Y. *et al.* Ultrafast hydrogen-ion storage in MoO_3 nanoribbons. *Solid State Ionics* **353**, 115380 (2020).
37. Ritter, Cl., Müller-Warmuth, W. & Schöllhorn, R. Structure and motion of hydrogen in molybdenum bronzes H_xMoO_3 as studied by nuclear magnetic resonance. *J. Chem. Phys.* **83**, 6130–6138 (1985).

38. Anne, M., Fruchart, D., Derdour, S. & Tinet, D. Structure of $D_{1.65}MoO_3$ by neutron diffraction. *Journal de Physique* **49**, 505–509 (1988).
39. Zhang, H. *et al.* Interlayer Engineering of α-MoO_3 Modulates Selective Hydronium Intercalation in Neutral Aqueous Electrolyte. *Angewandte Chemie International Edition* **60**, 896–903 (2021).
40. Jiang, H. *et al.* A High-Rate Aqueous Proton Battery Delivering Power Below −78°C via an Unfrozen Phosphoric Acid. *Advanced Energy Materials* **10**, 2000968 (2020).
41. Su, Z. *et al.* "Water-in-Sugar" Electrolytes Enable Ultrafast and Stable Electrochemical Naked Proton Storage. *Small* **17**, 2102375 (2021).
42. Tang, W. *et al.* An aqueous rechargeable lithium battery of excellent rate capability based on a nanocomposite of MoO_3 coated with PPy and $LiMn_2O_4$. *Energy & Environmental Science* **5**, 6909–6913 (2012).
43. Chu, Y. *et al.* In situ built interphase with high interface energy and fast kinetics for high performance Zn metal anodes. *Energy Environ. Sci.* **14**, 3609–3620 (2021).
44. Braïda, B., Adams, S. & Canadell, E. Concerning the Structure of Hydrogen Molybdenum Bronze Phase III. A Combined Theoretical–Experimental Study. *Chem. Mater.* **17**, 5957–5969 (2005).
45. Momma, K. & Izumi, F. VESTA 3 for three-dimensional visualization of crystal, volumetric and morphology data. *J Appl Cryst, J Appl Crystallogr* **44**, 1272–1276 (2011).
46. Kresse, G. & Furthmüller, J. Efficient iterative schemes for ab initio total-energy calculations using a plane-wave basis set. *Phys. Rev. B* **54**, 11169–11186 (1996).
47. Kresse, G. & Furthmüller, J. Efficiency of ab-initio total energy calculations for metals and semiconductors using a plane-wave basis set. *Computational Materials Science* **6**, 15–50 (1996).
48. Blöchl, P. E. Projector augmented-wave method. *Phys. Rev. B* **50**, 17953–17979 (1994).
49. Perdew, J. P., Burke, K. & Ernzerhof, M. Generalized Gradient Approximation Made Simple. *Phys. Rev. Lett.* **77**, 3865–3868 (1996).
50. Perdew, J. P., Burke, K. & Ernzerhof, M. Generalized Gradient Approximation Made Simple [Phys. Rev. Lett. 77, 3865 (1996)]. *Phys. Rev. Lett.* **78**, 1396–1396 (1997).
51. Grimme, S. Semiempirical GGA-type density functional constructed with a long-range dispersion correction. *Journal of Computational Chemistry* **27**, 1787–1799 (2006).
52. Rellán-Piñeiro, M. & López, N. One Oxygen Vacancy, Two Charge States: Characterization of Reduced α-MoO3(010) through Theoretical Methods. *J. Phys. Chem. Lett.* **9**, 2568–2573 (2018).
53. CHASE, M. W. NIST-JANAF Thermochemical tables 4th ed. *J. of Physical and Chemical Reffernce Data* 1529–1564 (1998).
54. Henkelman, G., Uberuaga, B. P. & Jónsson, H. A climbing image nudged elastic band method for finding saddle points and minimum energy paths. *J. Chem. Phys.* **113**, 9901–9904 (2000).

Figures

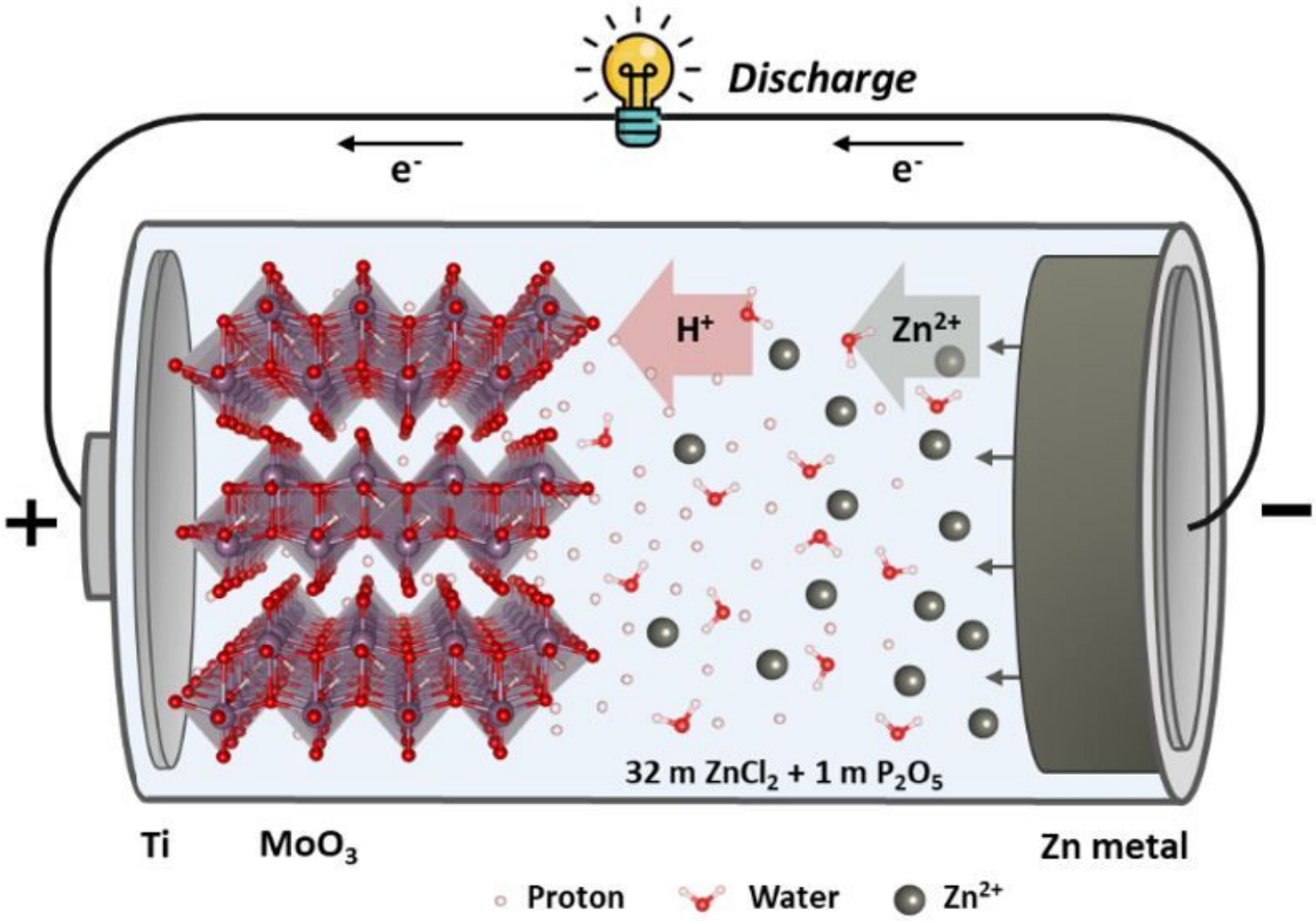

Figure 1

Schematic illustration of the aqueous dual-ion Zn^{2+}/H^{+} battery prototype. The battery consists of a H^{+} intercalation positive electrode α-MoO_3 and a Zn metal plating/stripping negative electrode with an aqueous dual-ion Zn^{2+}/H^{+} electrolyte.

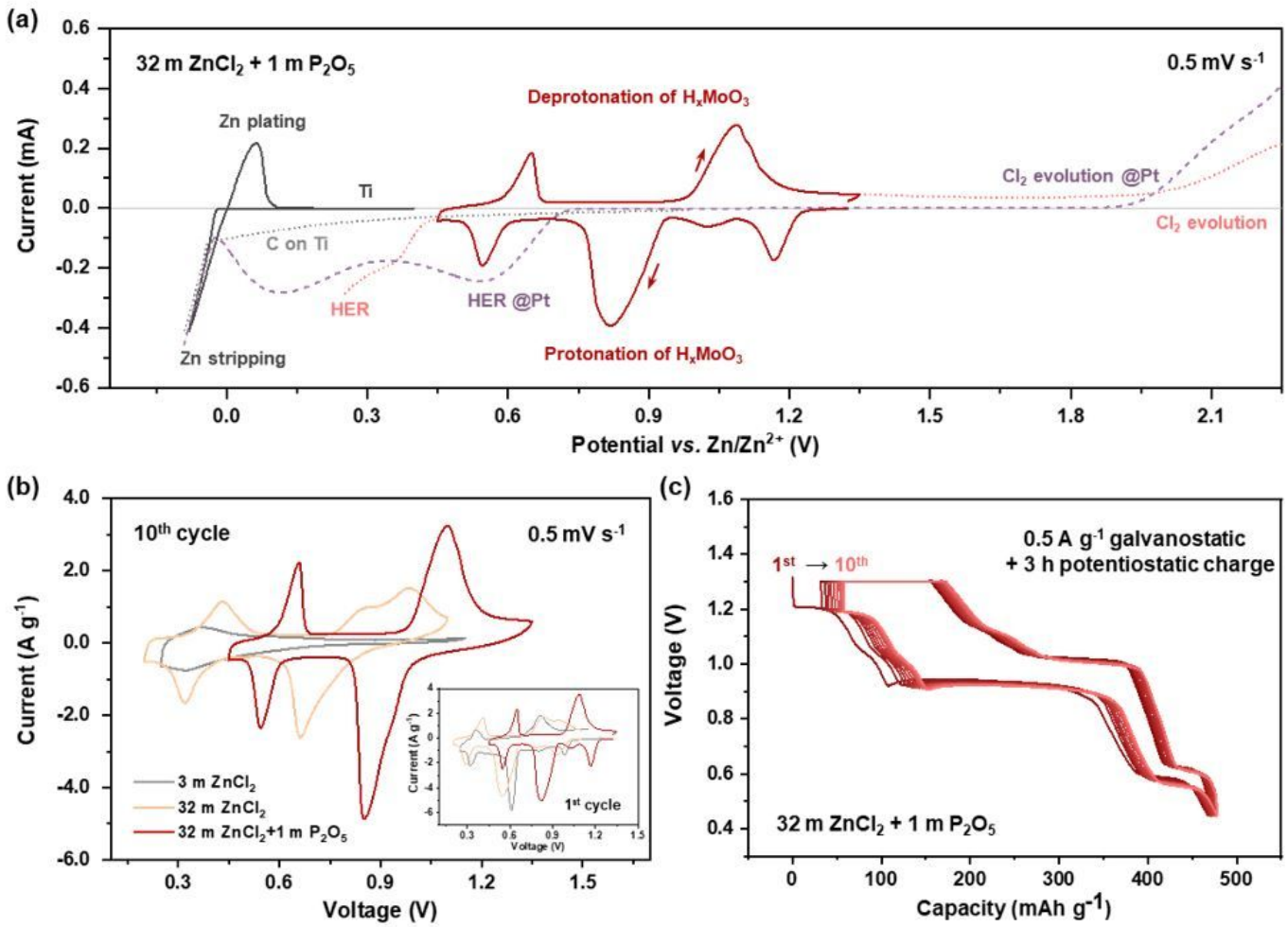

Figure 2

Electrochemical properties of α-MoO_3 in aqueous dual-ion Zn^{2+}/H^+ electrolytes. (a) CV curves of α-MoO_3 in a 32 m $ZnCl_2$ + 1 m P_2O_5 aqueous electrolyte (red solid line). The CV curve of Zn plating/stripping on a Ti current collector (gray solid line) and the LSV curves of hydrogen-evolution and chlorine evolution reactions on a Pt current collector are also shown for comparison (purple dash lines). The red dotted lines are the LSV curves using the α-MoO_3 electrode. The gray dotted line is the LSV curve using Ti foil coated with carbon. (b) The CV curves of α-MoO_3 during the 10^{th} cycle using 3 m $ZnCl_2$ (gray line), 32 m $ZnCl_2$ (orange line), and 32 m $ZnCl_2$ + 1 m P_2O_5 (red line) aqueous electrolytes. The inset shows the CV curves at the first cycle. (c) The charge/discharge curves of α-MoO_3 in a 32 m $ZnCl_2$ + 1 m P_2O_5 aqueous electrolyte under a galvanostatic + potentiostatic charging mode (A 3 h constant voltage of 1.3 V *vs.* Zn/Zn^{2+} was applied after each constant current charging at 0.5 A/g) , corresponding to H_xMoO_3 ($0 \leq x \leq 2.5$).

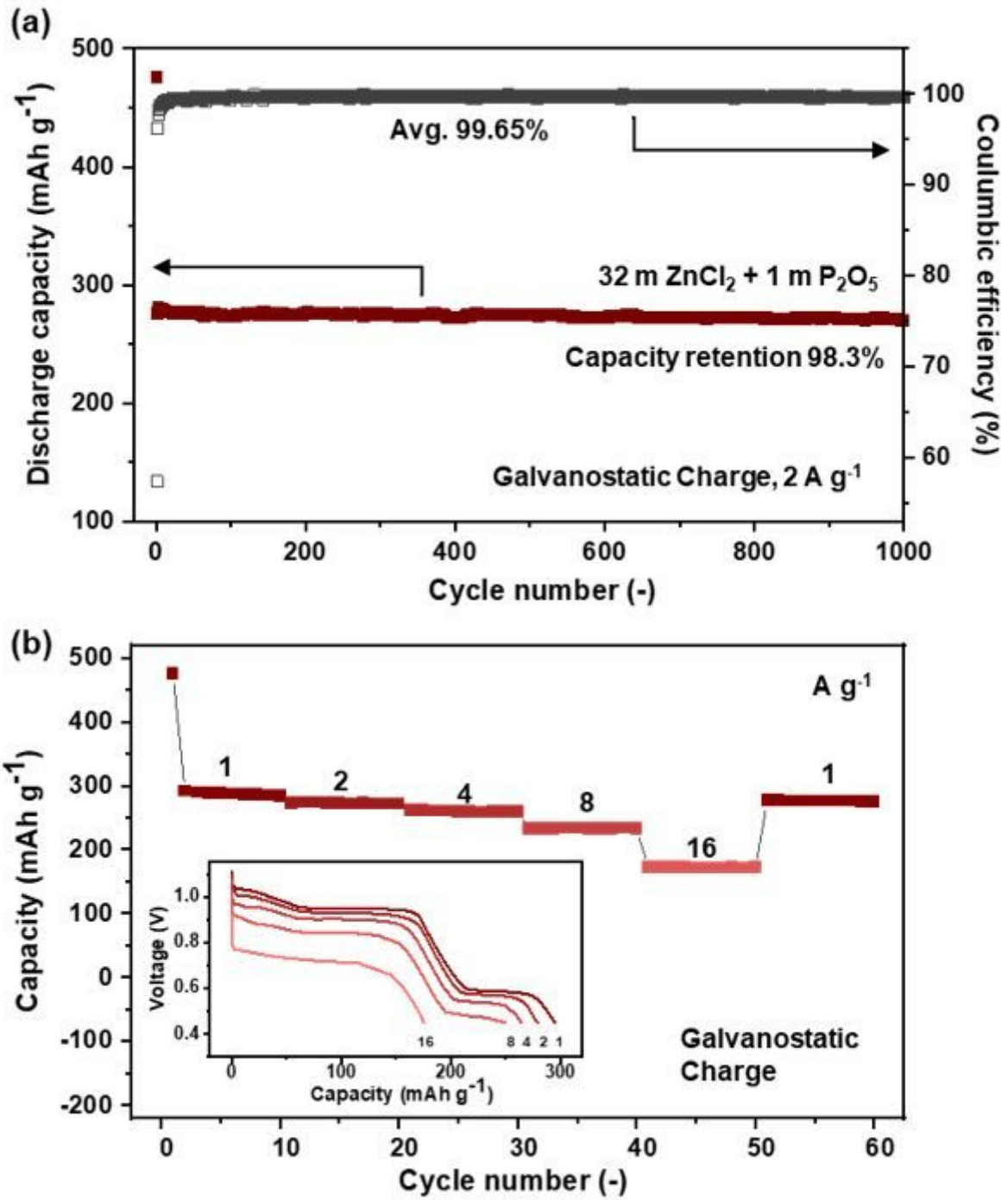

Figure 3

Cycle stability and rate capability of H_xMoO_3 ($1.0 \leq x \leq 2.5$) in Galvanostatic charge mode. (a) Discharge capacity and coulombic efficiency at 2 A g^{-1}, (b) rate performance at discharge rates from 1 A g^{-1} to 16 A g^{-1}. Inset: the corresponding discharge curves.

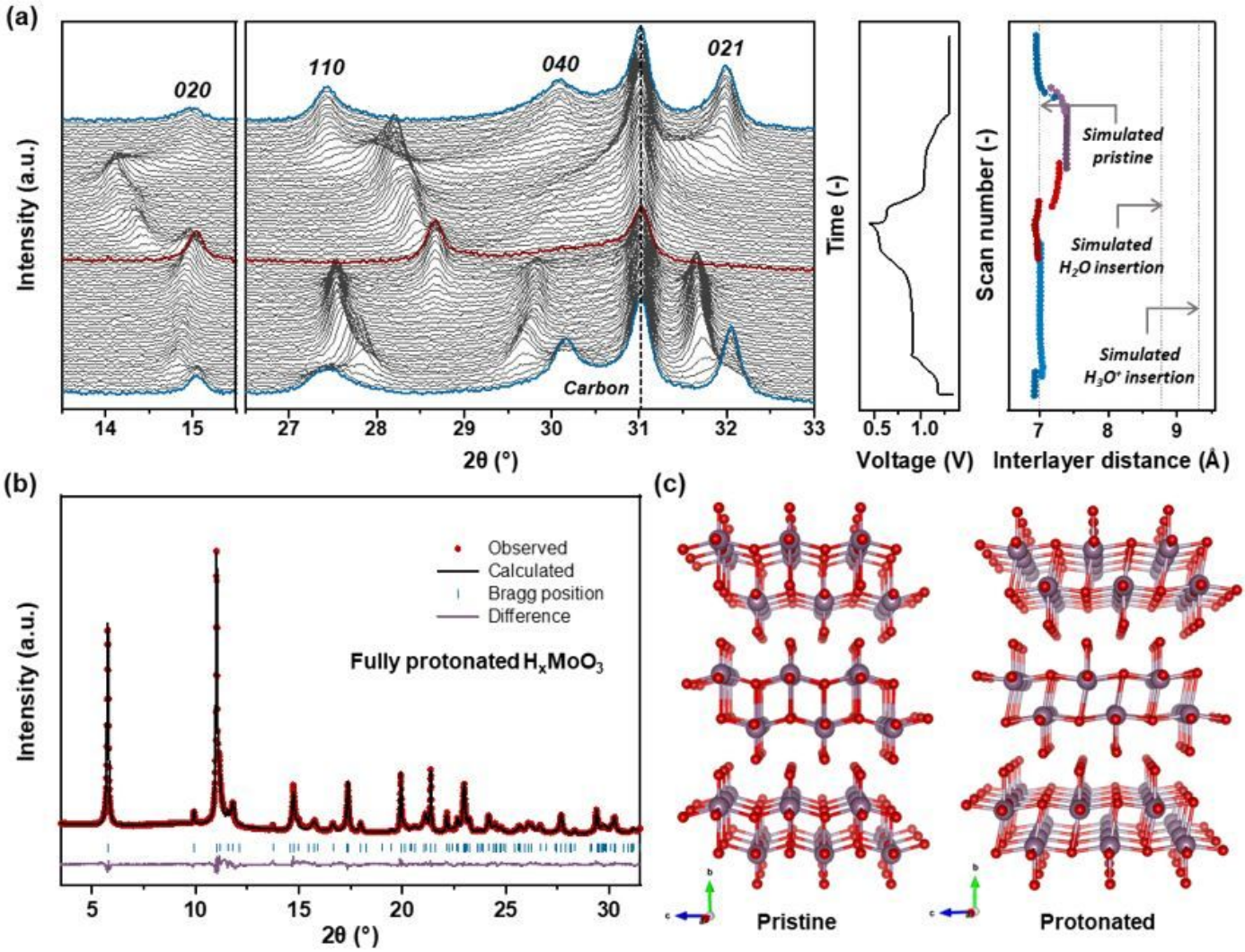

Figure 4

Structural evolution of MoO_3 upon (de)protonation. (a) *In situ* XRD patterns upon protonation and deprotonation of MoO_3, and deduced interlayer-distance change (colored dotted lines). The simulated interlayer distances of H_2O (1 H_2O in 16 MoO_3) or H_3O^+ (1 H_3O^+ in 16 MoO_3) intercalated MoO_3 are also indicated for comparison (gray dotted lines). (b) Synchrotron XRD pattern and the Rietveld refinement result of protonated $H_{2.5}MoO_3$. (c) Refined structures of pristine (left) and protonated (right) phases. Note that the proton positions cannot be determined by the synchrotron XRD and therefore are not shown.

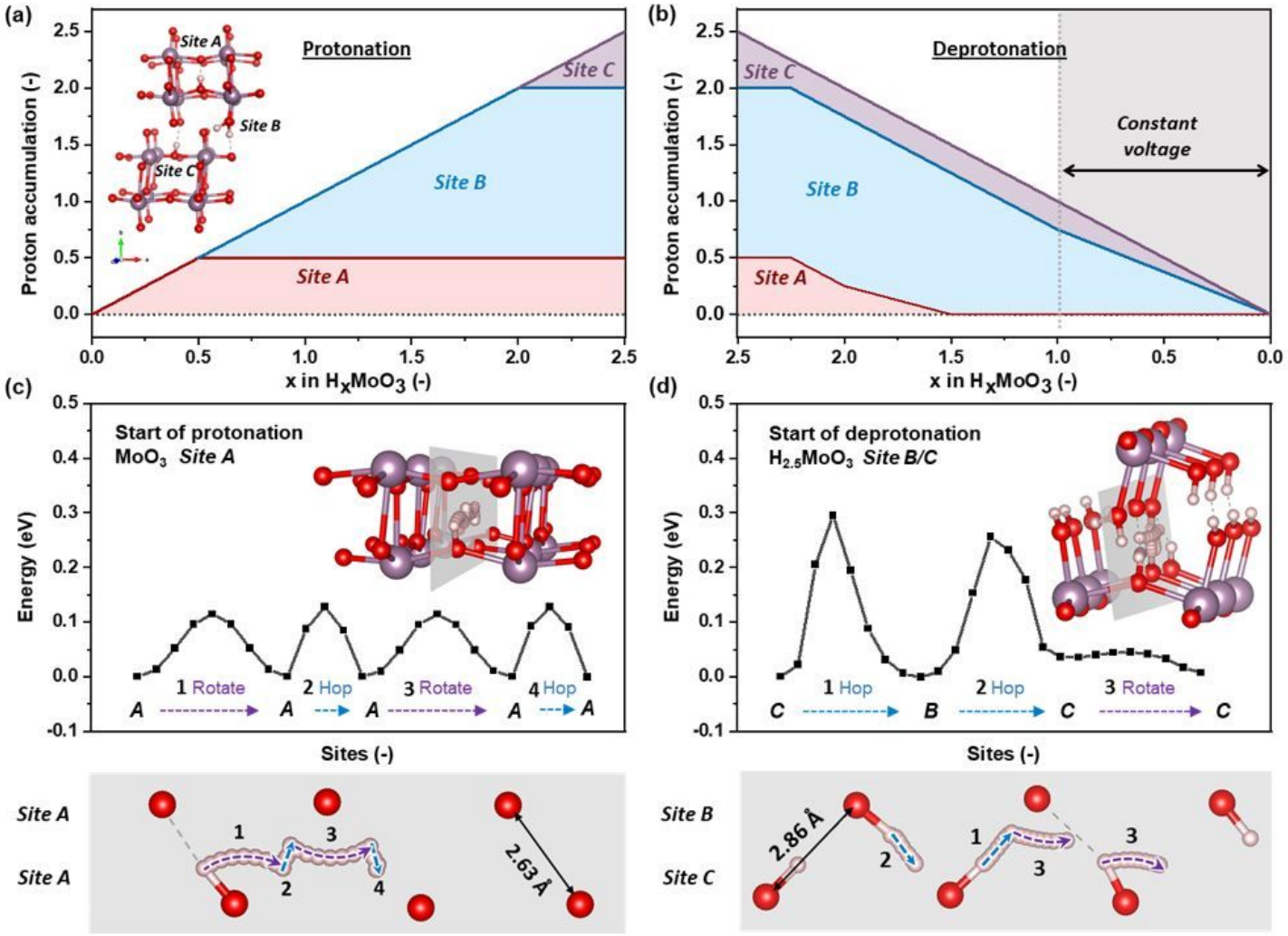

Figure 5

Solid-state anhydrous Grotthuss mechanism for fast proton transport in dense oxide-ion array. The occupancy of each site in (a) protonation with an order of site A (0.5 H^+) → site B (1.5 H^+) → site C (0.5 H^+), and (b) deprotonation with an order of site C (0.25 H^+) → site A (0.5 H^+) → site B (0.75 H^+) → site B + site C (1.0H^+). (c-d) Anhydrous Grotthuss mechanism for proton transport and corresponding energy barriers at the early stages of protonation (c) and deprotonation (d).

Supplementary Files

This is a list of supplementary files associated with this preprint. Click to download.

- SIv2MaMoO3NM.docx